2017

In vivo real-time imaging of cutaneous hemoglobin concentration, oxygen saturation, scattering properties, melanin content, and epidermal thickness with visible spatially modulated light

Xinlin Chen

Weihao Lin

Chenge Wang

Shaoheng Chen

Jing Sheng

See next page for additional authors

Peer Reviewed

Published Citation

Chen, X., Lin, W., Wang, C., Chen, S., Sheng, J., Zeng, B., & Xu, M. (2017). In vivo real-time imaging of cutaneous hemoglobin concentration, oxygen saturation, scattering properties, melanin content, and epidermal thickness with visible spatially modulated light. Biomedical optics express, 8(12), 5468-5482. doi:10.1364/BOE.8.005468.

Research Article | Vol. 8, No. 12 | 1 Dec 2017 | BIOMEDICAL OPTICS EXPRESS 5468
Biomedical Optics EXPRESS

In vivo real-time imaging of cutaneous hemoglobin concentration, oxygen saturation, scattering properties, melanin content, and epidermal thickness with visible spatially modulated light

XINLIN CHEN,[1] WEIHAO LIN,[1] CHENGE WANG,[1] SHAOHENG CHEN,[1] JING SHENG,[1] BIXIN ZENG,[1] AND M. XU[1,2,*]

[1]*Institute of Lasers and Biomedical Photonics, Biomedical Engineering College, Wenzhou Medical University, Wenzhou, Zhejiang, 325035, China*
[2]*Dept. of Physics, Fairfield University, 1073 North Road, Fairfield, CT 06824, USA*
[*]*mxu@fairfield.edu*

Abstract: We present the real-time single snapshot multiple frequency demodulation - spatial frequency domain imaging (SSMD-SFDI) platform implemented with a visible digital mirror device that is capable of imaging and monitoring dynamic turbid medium and processes over a large field of view. One challenge in quantitative imaging of biological tissue such as the skin is the complex structure rendering techniques based on homogeneous medium models to fail. To address this difficulty we have also developed a novel method that maps the layered structure to a homogeneous medium for spatial frequency domain imaging. The varying penetration depth of spatially modulated light on its wavelength and modulation frequency is used to resolve the layered structure. The efficacy of the real-time SSMD-SFDI platform and this two-layer model is demonstrated by imaging forearms of 6 healthy subjects under the reactive hyperemia protocol. The results show that our approach not only successfully decouples light absorption by melanin from that by hemoglobin and yields accurate determination of cutaneous hemoglobin concentration and oxygen saturation, but also provides reliable estimation of the scattering properties, the melanin content and the epidermal thickness in real time. Potential applications of our system in imaging skin physiological and functional states, cancer screening, and microcirculation monitoring are discussed at the end.

OCIS codes: (110.0110) Imaging systems; (110.0113) Imaging through turbid media; (170.3880) Medical and biological imaging.

References and links

1. T. W. L. Scheeren, P. Schober, and L. A. Schwarte, "Monitoring tissue oxygenation by near infrared spectroscopy (NIRS): Background and current applications," J. Clin. Monit. Comput. **26**(4), 279–287 (2012).
2. M. Mogensen, L. Thrane, T. M. Jørgensen, P. E. Andersen, and G. B. E. Jemec, "OCT imaging of skin cancer and other dermatological diseases," J. Biophotonics **2**(6-7), 442–451 (2009).
3. M. Balu, "*In-vivo* multiphoton microscopy (MPM) of laser-induced optical breakdown (LIOB) in human skin (Conference Presentation)," in *Proceedings of International Society for Optics and Photonics*, vol. 10037, (Academic, 2017), pp. 100370F.
4. S. G. Sagraves, "Tissue oxygenation monitoring in the field: a new EMS vital sign," J. Trauma **67**(3), 441–444 2009.
5. S. B. Chakravarti, A. J. C. Mittnacht, J. C. Katz, K. Nguyen, U. Joashi, and S. Srivastava, "Multisite near-infrared spectroscopy predicts elevated blood lactate level in children after cardiac surgery," J. Cardiothorac. Vasc. Anesth. **23**(5), 663–667 (2009).
6. J. M. Kainerstorfer, A. Sassaroli, K. T. Tgavalekos, and S. Fantini, "Cerebral autoregulation in the microvasculature measured with near-infrared spectroscopy," J. Cereb. Blood Flow Metab. **35**(6), 959–966 (2015).

#305430 https://doi.org/10.1364/BOE.8.005468
Journal © 2017 Received 24 Aug 2017; revised 20 Oct 2017; accepted 24 Oct 2017; published 8 Nov 2017

Biomedical Optics EXPRESS

7. I. Tachtsidis, M. M. Tisdall, C. Pritchard, T. S. Leung, C. E. Elwell, and M. Smith, "Hemoglobin and myoglobin contributions to skeletal muscle oxygenation in response to exercise," J. Adv. Exp. Med Biol. **701**(2), 347–352 (2011).
8. F. R. Ayers, D. J. Cuccia, K. M. Kelly, and A. J. Durkin, "Wide-field spatial mapping of *in vivo* tattoo skin optical properties using modulated imaging," Lasers Surg. Med. **41**(6), 442–453 (2009).
9. M. R. Pharaon, "Early detection of complete venous occlusion in a rodent and swine pedicle flap model using modulated imaging, a new novel multispectral imaging technique," J. Am. Coll. Surg. **209**(3), S77–S78 (2009).
10. D. J. Cuccia, F. Bevilacqua, A. J. Durkin, and B. J. Tromberg, "Modulated imaging: quantitative analysis and tomography of turbid media in the spatial-frequency domain," Opt. Lett. **30**(11), 1354–1356 (2005).
11. J. R. Weber, D. J. Cuccia, A. J. Durkin, and B. J. Tromberg, "Noncontact imaging of absorption and scattering in layered tissue using spatially modulated structured light," J. Appl. Phys. **105**(10), 1–9 (2009).
12. B. Yang, "Color structured light imaging of skin," J. Biomed. Opt. **5**(10), 050503 (2016).
13. C. Fink and H. A. Haenssle, "Non-invasive tools for the diagnosis of cutaneous melanoma," J. Ski. Res. Technol. **5**, 1–11 (2016).
14. D. J. Cuccia, F. Bevilacqua, A. J. Durkin, F. R. Ayers, and B. J. Tromberg, "Quantitation and mapping of tissue optical properties using modulated imaging," J. Biomed. Opt. **14**(2), 024012 (2009).
15. M. Ghijsen, B. Choi, A. J. Durkin, S. Gioux, and B. J. Tromberg, "Real-time simultaneous single snapshot of optical properties and blood flow using coherent spatial frequency domain imaging (cSFDI)," Biomed. Opt. Express **7**(3), 870–882 (2016).
16. N. Mackinnon, "Separating melanin from hemodynamics in nevi using multimode hyperspectral dermoscopy and spatial frequency domain spectroscopy," J. Biomed. Opt. **21**(11), 114001 (2016).
17. X. Chen, Z. Cao, W. Lin, Z. Zhu, B. Zeng and M. Xu, "Microcirculation monitoring with real time spatial frequency domain imaging," in *Int. Conf. Innov. Opt. Heal. Sci*., vol. 10245, (China, 2017), pp. 102450J.
18. M. Xu, Z. Cao, W. Lin, X. Chen, L. Zheng, and B. Zeng, "Single snapshot multiple frequency modulated imaging of subsurface optical properties of turbid media with structured light," AIP Adv. **6**(12), (2016).
19. J. B. Travers, C. Poon, D. J. Rohrbach, N. M. Weir, E. Cates, F. Hager, and U. Sunar, "Noninvasive mesoscopic imaging of actinic skin damage using spatial frequency domain imaging," Biomed. Opt. Express **8**(6), 3045–3052 (2017).
20. M. Xu, "Diagnosis of the phase function of random media from light reflectance," Sci. Rep. **6**, 22535, (2016).
21. M. Xu, "Low-coherence enhanced backscattering beyond diffusion," Opt. Lett. **33**(11), 1246–1248 (2008).
22. M. Reilly and M. Xu, "Analytical model for sub-diffusive light reflection and the application to spatial frequency-domain imaging," Proc. SPIE **9319**, 93191A (2015).
23. D. J. Rohrbach, D. Muffoletto, J. Huihui, R. Saager, K. Keymel, A. Paquette, J. Morgan, N. Zeitouni, and U. Sunar, "Preoperative mapping of nonmelanoma skin cancer using spatial frequency domain and ultrasound imaging," Acad. Radiol. **21**(2), 263–270 (2014).
24. D. J. Rohrbach, N. C. Zeitouni, D. Muffoletto, R. Saager, B. J. Tromberg, and U. Sunar, "Characterization of nonmelanoma skin cancer for light therapy using spatial frequency domain imaging," Biomed. Opt. Express **6**(5), 1761–1766 (2015).
25. A. Yafi, F. K. Muakkassa, T. Pasupneti, J. Fulton, D. J. Cuccia, A. Mazhar, K. N. Blasiole, and E. N. Mostow, "Quantitative skin assessment using spatial frequency domain imaging (SFDI) in patients with or at high risk for pressure ulcers," Lasers Surg. Med. **49**(9), 827–834 (2017).
26. R. B. Saager, A. J. Durkin, K. M. Kelly, and B. J. Tromberg, "*In vivo* measurements of cutaneous melanin across spatial scales: using multiphoton microscopy and spatial frequency domain spectroscopy," J. Biomed. Opt. **20**, 066005 (2015).
27. D. Yudovsky, J. Q. M. Nguyen, and A. J. Durkin, "*In vivo* spatial frequency domain spectroscopy of two layer media," J. Biomed. Opt. **17**(10), 107006 (2012).
28. R. B. Saager, A. Truong, D. J. Cuccia, and A. J. Durkin, "Method for depth-resolved quantitation of optical properties in layered media using spatially modulated quantitative spectroscopy," J. Biomed. Opt. **16**(7), 077002 (2011).
29. M. Xu, "Plum pudding random medium model of biological tissue toward remote microscopy from spectroscopic light scattering," Biomed. Opt. Express **8**(6), 2879–2895 (2017).
30. M. Xu, T. T. Wu, and J. Y. Qu, "Unified Mie and fractal scattering by cells and experimental study on application in optical characterization of cellular and subcellular structures," J. Biomed. Opt. **13**(2), 024015 (2008).
31. M. Xu and R. R. Alfano, "Fractal mechanisms of light scattering in biological tissue and cells," Opt. Lett. **30**(22), 3051–3053 (2005).
32. T. T. Wu, J. Y. Qu, and M. Xu, "Unified Mie and fractal scattering by biological cells and subcellular structures," Opt. Lett. **32**(16), 2324–2326 (2007).
33. A. Hennessy, C. Oh, B. Diffey, K. Wakamatsu, S. Ito, and J. Rees, "Eumelanin and pheomelanin concentrations in human epidermis before and after UVB irradiation," Pigment Cell Res. **18**(3), 220–223 (2005).
34. S. Alaluf, D. Atkins, K. Barrett, M. Blount, N. Carter, and A. Heath, "Ethnic variation in melanin content and composition in photoexposed and photoprotected human skin," Pigment Cell Res. **15**(2), 112–118 (2002).
35. T. Sarna and H. M. Swartz, *The Pigmentary System* (Oxford University Press, 1988). The physical properties of melanins.

Biomedical Optics EXPRESS

36. M. Xu, "Electric field Monte Carlo simulation of polarized light propagation in turbid media," Opt. Express **12**(26), 6530–6539 (2004).
37. A. N. Bashkatov, E. A. Genina, and V. V. Tuchin, "Optical properties of skin, subcutaneous, and muscle tissues: a review," J. Innov. Opt. Health Sci. **4**(1), 9–38 (2011).
38. T.-Y. Tseng, C.-Y. Chen, Y.-S. Li, and K.-B. Sung, "Quantification of the optical properties of two-layered turbid media by simultaneously analyzing the spectral and spatial information of steady-state diffuse reflectance spectroscopy," Biomed. Opt. Express **2**(4), 901–914 (2011).
39. K. Wasserman, "The anaerobic threshold: definition, physiological significance and identification," Adv. Cardiol. **35**(1), 1–23 (1986).
40. A. A. Nurmatov, A. V. Samoĭlenko, and B. I. Tkachenko, "Systemic hemodynamic shifts in the arterial and venous portions of the vascular bed in hypoxia," Fiziologicheski Zhurnal SSSR Imeni I.m.sechenova **72**(11), 1515 (1986).
41. C. B. Wolff, "Normal cardiac output, oxygen delivery and oxygen extraction," Adv. Exp. Med. Biol. **599**, 169–182 (2007).
42. T. Wang, *Evolution of the Cardiovascular Autonomic Nervous System in Vertebrates*, 3rd ed. (Elsevier Inc., 2012).
43. P. O'Herron, P. Y. Chhatbar, M. Levy, Z. Shen, A. E. Schramm, Z. Lu, and P. Kara, "Neural correlates of single-vessel haemodynamic responses *in vivo*," Nature **534**(7607), 378–382 (2016).
44. A. Sitek, I. Rosset, E. Żądzińska, A. Kasielska-Trojan, A. Neskoromna-Jędrzejczak, and B. Antoszewski, "Skin color parameters and Fitzpatrick phototypes in estimating the risk of skin cancer: a case-control study in the Polish population," J. Am. Acad. Dermatol. **74**(4), 716–723 (2016).
45. M. Mackiewicz-Wysocka, A. Araszkiewicz, J. Schlaffke, S. Kuczynski, I. Micek, and D. Zozulinska-Ziolkiewicz, "Lower melanin content in the skin of type 1 diabetic patients and the risk of microangiopathy," Exp. Clin. Endocrinol. Diabetes **122**(4), 231–235 (2014).

1. Introduction

The skin is the largest organ of the body, accounting for about 15% of the total adult body weight. Besides providing the mechanical barrier to protect the surface of the body and to prevent water loss, it has other important functions in sensory perception, inflammation, hemostasis and wound healing. Monitoring skin anatomy and physiology is hence essential in dermatology. Optical methods for characterizing skin structure and hemodynamics have been long pursued due to some important advantages including non-invasiveness, high sensitivity to hemoglobin, and low cost [1].

Confocal reflectance imaging, optical coherence tomography (OCT) [2], and multi-photon microscopy (MPM) [3] provide high-resolution (e.g., 1–10 μm) structural images of skin with optical sectioning capability and limited penetration depth (e.g., 100 μm–1mm). These techniques, however, are limited to mainly morphology and are unable to assess hemodynamics or provide useful physiological information on microcirculation. Near infrared spectroscopy (NIRS), on the other hand, has been widely used for the measurement of cutaneous hemodynamics-related physiological parameters [4] in such as trauma care [5], cardiac surgery [6], non-cardiac surgery [7], and skin examination in general. One main drawback of NIRS is that it requires a prior knowledge of the scattering property of the specimen. The accuracy of the recovered hemodynamics parameters may be significantly affected by improper assumption in the scattering properties. As a point detection method, NIRS will also require scanning to form an image.

These two drawbacks of NIRS have been overcome by the emerging Spatial Frequency Domain Imaging (SFDI) [8–10]. SFDI is a novel non-contact optical imaging technology with the unique capability of allowing wide-field quantitative mapping of tissue optical properties [10–12] (absorption and scattering coefficients) and physiological parameters [12–16] including oxygenated hemoglobin concentration and deoxygenated hemoglobin concentration. SFDI uses patterned illumination for imaging tissue over a large field of view [17, 18]. The reflectance of spatially-modulated waves is first demodulated to compute the tissue modulation transfer function (MTF) from which the optical properties are then determined by comparing to appropriate light migration models [19–22].

Recently, the application of SFDI in skin imaging has attracted significant attention. Rohrbach et al applied SFDI to image the skin optical and vascular parameters of nonmelanoma skin cancer patients [23, 24]. Yafi et al studied the feasibility of SFDI for

Biomedical Optics EXPRESS

pressure ulcer staging and a homogenous Monte Carlo tissue model was used to recover the optical properties [25]. Saager et al used Spatial frequency Domain Spectroscopy (SFDS) over the spectral range of 450-1000 nm to separate melanin from hemoglobin and recover more reliably the cutaneous hemoglobin concentration and oxygen saturation taking into account the two-layer structure of skin [26].

There are, however, still significant challenges in the application of SFDI in skin imaging. Skin is highly structured and layered. Chromophores such as melanin are typically confined within the epidermis whereas hemoglobin is confined within the dermis beneath. Accounting for the two-layer structure has been found to be critical to the accurate recovery of hemoglobin concentration and oxygen saturation [27]. The difference in the penetration of light into the skin within visible and infrared spectral ranges has been used to separate light absorption by melanin from that by hemoglobin and estimate the epidermal thickness [26]. Nevertheless the method is slow (10 to 40 seconds for measurement at one point) and cannot be applied in real-time imaging. A rapid optical imaging modality for quantifying the skin two-layer structure and microcirculation is thus much desired. Real-time imaging is also advantageous in suppressing motion artifacts and needed for the characterization and monitoring of non-static media.

In this article, we present a real-time Single Snapshot Multiple Frequency Demodulation - Spatial Frequency Domain Imaging (SSMD-SFDI) platform implemented with a visible digital mirror device to map the optical properties of the subsurface of the skin continuously. Unlike conventional SFDI utilizing three-phase demodulation from three images acquired at different phase delays, single snapshot multiple frequency demodulation (SSMD) [18] is capable of extracting multiple modulation transfer functions (MTF) from a single structured light image containing multiple components of different spatial modulation frequencies. The SSMD-SFDI platform is suitable for imaging and monitoring dynamic turbid medium and processes over a large field of view. We also present a novel method that maps the layered structure to a homogeneous medium for spatial frequency domain imaging. The varying penetration depth of spatially modulated light on its wavelength and modulation frequency is used to resolve the layered structure. In the context of skin imaging, this method not only successfully decouples light absorption by melanin from that by hemoglobin and yields accurate determination of hemoglobin concentration and oxygen saturation, but also provides reliable estimation of scattering properties, the melanin content and the epidermal thickness. The efficacy of the real-time SSMD-SFDI platform and this layered model is demonstrated by imaging forearms of 6 healthy subjects under the reactive hyperemia protocol. Potential applications of our system in imaging skin physiological and functional states, cancer screening, and microcirculation monitoring are discussed at the end of the article.

2. Materials and methods

2.1 SSMD-SFDI

SFDI is a non-contact optical imaging technology with the unique capability of allowing wide-field quantitative mapping of tissue optical properties (absorption and scattering coefficients). In SFDI, the incident spatially modulated light comprises a DC component, $I_{DC}^{(0)}$, and an AC component, $I_{AC}^{(0)}\cos(2\pi fx+\phi)$, modulated at a specific frequency *f*. The reflectance of the spatially-modulated light is demodulated to obtain the tissue modulation transfer function. Conventional SFDI utilizes a demodulation technique referred to as the three-phase method and requires three images $I_{0^\circ}, I_{120^\circ}, I_{240^\circ}$ acquired at different phase delays (0, 2π/3, and 4π/3) to compute MTF (the ratio of I_{AC} and $I_{AC}^{(0)}$) at one spatial frequency:

$$I_{AC}=\frac{\sqrt{2}}{3}\sqrt{\left(I_{0^\circ}-I_{120^\circ}\right)^2+\left(I_{120^\circ}-I_{240^\circ}\right)^2+\left(I_{240^\circ}-I_{0^\circ}\right)^2}. \quad (1)$$

Biomedical Optics EXPRESS

In contrast, the recently proposed single snapshot multiple frequency demodulation (SSMD) method [18] can extract multiple modulation transfer functions from a single structured light image containing multiple components of different spatial modulation frequencies. The amplitude of the *i*-th AC component is given by

$$I_{AC,i} = \frac{\sqrt{[\iint_{\sigma} I(x,y)\cos(2\pi f_{x,i}x + 2\pi f_{y,i}y)dxdy]^2 + [\iint_{\sigma} I(x,y)\sin(2\pi f_{x,i}x + 2\pi f_{y,i}y)dxdy]^2}}{\iint_{\sigma} \cos^2(2\pi f_{x,i}x + 2\pi f_{y,i}y)dxdy}. \quad (2)$$

where $(f_{x,i}, f_{y,i})$ is the spatial frequency of the *i*-th spatial modulation pattern and σ represents the kernel window of an appropriate size over which the integration is being performed [18]. The optical properties of the specimen are assumed to vary slowly over the kernel window in SSMD. When the kernel size is larger than the scale over which the optical properties of the medium vary, SSMD may lead to a sacrifice in the spatial resolution and introduce error [18].

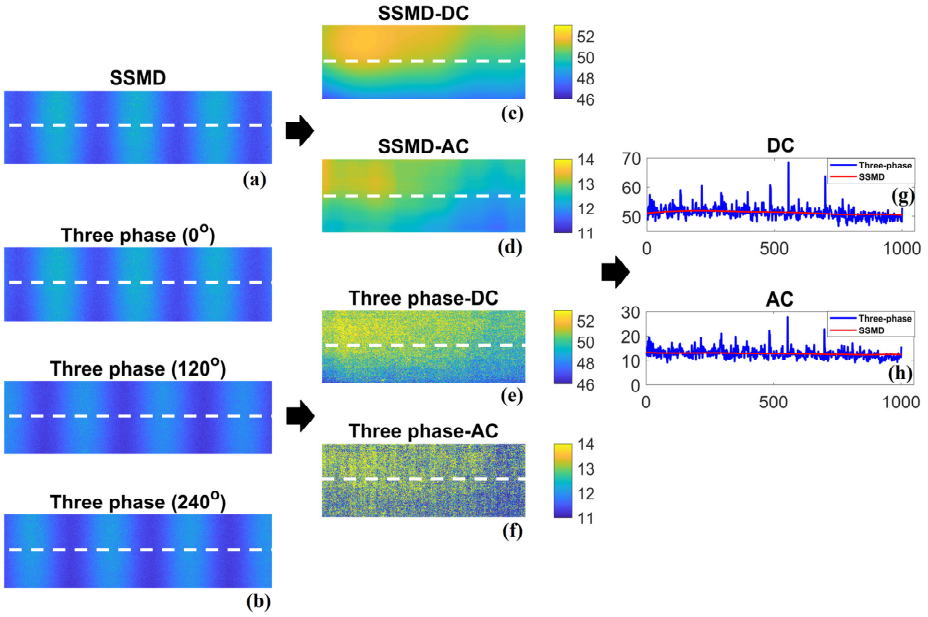

Fig. 1. Comparison of SSMD and the three-phase demodulation methods. See text.

The comparison of SSMD and the three-phase demodulation methods is shown in Fig. 1 for one typical measurement result on a solid phantom (Biomimic, Canada). SSMD can extract both AC and DC components (Fig. 1(c), 1(d)) from a single structured light image (Fig. 1(a)) whereas conventional three phase demodulation requires three images (Fig. 1(b)) to extract AC and DC components (Fig. 1(e), 1(f)). Both three phase and SSMD methods produce similar demodulated images but the SNR in SSMD is much higher (Fig. 1(g), 1(h), SSMD: red line, three phase demodulation: blue line).

2.2 Mapping a two-layer structure to an effective homogeneous medium in SFDI

Biological tissue such as the skin is highly structured. The skin consists of three main visible layers from the surface: epidermis (~100μm thick, the blood-free layer), dermis (1–4mm thick, vascularized layer) and subcutaneous fat (from 1 to 6mm thick, in dependence from the body site). The main absorbers in the visible and near infrared spectral range are melanin typically confined within the epidermis and hemoglobin located within the dermis beneath. Light penetration is mostly confined within the top two (epidermis and dermis) layers in

Biomedical Optics EXPRESS

reflection measurements such as SFDI. Accounting for the two-layer structure has been found to be critical to the accurate recovery of cutaneous hemoglobin concentration and oxygen saturation [27, 28]. To this end, we have developed a novel approach that maps the two-layer structure to a homogeneous medium for spatial frequency domain imaging. The varying penetration depth of spatially modulated light on its wavelength and modulation frequency is used to resolve the two-layer structure.

Recognizing that the epidermis is much thinner and light is mostly collimated after passing through the epidermis, one could ignore the difference in the scattering property between the epidermis and dermis and further assume that the light absorption is different with the epidermis dominated by melanin and the dermis by oxy- and deoxyhemoglobins. The same assumption was made in earlier works [27, 28]. The absorption coefficients within the epidermis and dermis are given by

$$\mu_{a,epidermis}(\lambda) = \varepsilon_{melanin}(\lambda) c_{melanin}, \tag{3}$$

and

$$\mu_{a,dermis}(\lambda) = \varepsilon_{Hb}(\lambda) c_{Hb} + \varepsilon_{HbO_2}(\lambda) c_{HbO}, \tag{4}$$

respectively. Here $\varepsilon_{HbO_2}, \varepsilon_{Hb}, \varepsilon_{melanin}$ are the molar extinction coefficients of oxygenated hemoglobin, deoxygenated hemoglobin, and melanin, respectively; and $c_{HbO_2}, c_{Hb}, c_{melanin}$ are the concentrations of oxygenated hemoglobin, deoxygenated hemoglobin, and melanin, respectively.

The mapped homogeneous medium has the same reduced scattering coefficient $\mu_s'(\lambda)$ as the original medium and an effective absorption coefficient $\mu_a(\lambda)$ determined by requiring light absorption is equivalent within the two systems, i.e.,

$$\mu_a L = \mu_{a,epidermis}(\lambda) h + \mu_{a,dermis}(\lambda)(L-h), \tag{5}$$

where h is the epidermal thickness and L is the mean penetration depth for the modulated light at the spatial frequency f.

The reflectance of collimated modulated light from a homogeneous medium can be written as the summation from all layers at the depth z as $I(\mathrm{q}) = \int_0^\infty I(\mathrm{q}, z)\, dz$ where $\mathrm{q} = 2\pi f$ and the interface is at $z = 0$. The contribution from one layer at z is given by [20, 21]:

$$I(\mathrm{q}, z) = \frac{1}{4\pi} \mu_s'^2 \int_0^{+\infty} dz' \int_0^{+\infty} dz'' \exp\left[-\mu_t'(z' + z'')\right] g(\mathrm{q}, z, z')\, g(\mathrm{q}, z, z'') \tag{6}$$

where

$$g(\mathrm{q}, z, z') = \frac{1}{2QD_0} e^{-Q|Z-Z'|} - \frac{1}{2QD_0} \frac{1-Ql}{1+Ql} e^{-Q(z+z')}, \tag{7}$$

$\mu_t' \equiv \mu_a + \mu_s'$, $Q \equiv \sqrt{q^2 + 3\mu_a(\mu_a + \mu_s')}$, $D_0 = 1/3\mu_s'$, and l is the extrapolation length for diffusing light. The average penetration depth is then evaluated to be

$$L(\mathbf{q}, \lambda) = \frac{\int z I(\mathbf{q}, z)\, dz}{\int I(\mathbf{q}, z)\, dz} = \frac{(1+Ql)^2 (2\mu_t')^{-2} + (1+\mu_t' l)^2 (2Q)^{-2} - 2(1+Ql)(1+\mu_t' l)(Q+\mu_t')^{-2}}{(1+Ql)^2 (2\mu_t')^{-1} + (1+\mu_t' l)^2 (2Q)^{-1} - 2(1+Ql)(1+\mu_t' l)(Q+\mu_t')^{-1}}. \tag{8}$$

Biomedical Optics EXPRESS

The mapped absorption coefficient (and the mean penetration) can then be solved from the set of Eqs. (5) and (8). Equation (5) can be rewritten as

$$\mu_a = \mu_{a,dermis} + \left(\mu_{a,epidermis} - \mu_{a,dermis}\right)\frac{h}{L}. \tag{9}$$

A straightforward strategy is to iterate Eq. (9) with the initial μ_a set to $\mu_{a,dermis}$. The solution typically converges within 0.01% relative error after 10 iterations.

To complete the two-layer skin model, we will further assume light scattering by the epidermis and dermis is dominated by the fractal refractive index fluctuation [29–32]. Consequently, the reduced scattering coefficient takes the form of

$$\mu_s'(\lambda) = \mu_s'(540\text{ nm})\left(\frac{\lambda}{540\text{ nm}}\right)^{-b}. \tag{10}$$

where b is the scattering power and λ is the wavelength in nanometers. The melanin content and composition varies with ethnicity [33, 34]. For the subjects of Asian ethics investigated in this study, a composition of 95% eumelanin and 5% phemelanin was assumed. The molar extinction coefficients of oxygenated hemoglobin, deoxygenated hemoglobin and melanin at the three wavelengths (623 nm, 540 nm and 460 nm) taking into account the spectral profile of light source are summarized in Table 1 [35].

Table 1. The molar extinction coefficients of oxygenated hemoglobin, deoxygenated hemoglobin and melanin at the three wavelengths (623 nm, 540 nm and 460 nm).

	oxygenated hemoglobin (mm^{-1}/mM)	deoxygenated hemoglobin (mm^{-1}/mM)	melanin (mm^{-1}/mM)
λ = 623nm	0.0837	0.6130	0.1174
λ = 540nm	4.2139	4.4745	0.1966
λ = 460nm	4.4320	2.7876	0.3169

2.3 Color correction

The DMD projects white light comprising three components (RGB) of wavelengths of 623 nm, 540 nm and 460 nm, respectively. Each channel of the color image recorded by the digital camera is contaminated by its nonzero response to other colors. Therefore, it is necessary to perform channel unmixing to clean the measured light intensity when white light is used for illumination.

The response function of the digital camera can be measured by projecting the monochromatic (R, G, B) flat images in sequence on a Lambertian reflection standard. The camera records the channel averages (r_1, g_1, b_1) for red light, (r_2, g_2, b_2) for green light, and (r_3, g_3, b_3) for blue light after removing the dark current. The response function of the digital camera can now be written as

$$P = \begin{bmatrix} r_1 & r_2 & r_3 \\ g_1 & g_2 & g_3 \\ b_1 & b_2 & b_3 \end{bmatrix}. \tag{11}$$

Under the illumination of white light, the recorded intensity (R_{mix}, G_{mix}, B_{mix}) is related to the real light intensity (R_{raw}, G_{raw}, B_{raw}) via:

Biomedical Optics EXPRESS

$$P\begin{bmatrix} R_{raw} \\ G_{raw} \\ B_{raw} \end{bmatrix} = \begin{bmatrix} R_{mix} \\ G_{mix} \\ B_{mix} \end{bmatrix}. \tag{12}$$

The corrected light intensity is given by:

$$\begin{bmatrix} R_{raw} \\ G_{raw} \\ B_{raw} \end{bmatrix} = P^{-1}\begin{bmatrix} R_{mix} \\ G_{mix} \\ B_{mix} \end{bmatrix}. \tag{13}$$

The above correction is critical for the accurate determination of modulation transfer functions when white light is being used in measurement. Table 2 shows a typical case of SFDI imaging of a solid phantom. Excellent agreement is achieved between MTFs at the spatial frequency 0 and 0.2 mm^{-1} obtained with monochromatic and white light illumination after correction.

Table 2. Color correction under white light illumination.

		R channel		G channel		B channel	
		MTF_{DC}	MTF_{AC}	MTF_{DC}	MTF_{AC}	MTF_{DC}	MTF_{AC}
monochromatic light	SSMD	0.1524	0.0447	0.1477	0.0472	0.1389	0.0485
	Three-phase	0.1529	0.0438	0.1483	0.0464	0.1397	0.0474
white light	SSMD	0.1522	0.0451	0.1479	0.0469	0.1403	0.0482
	Three-phase	0.1527	0.0442	0.1484	0.0460	0.1409	0.0472

2.4 Experiment procedure and data analysis

The schematic diagram for the SSMD-SFDI system is shown in Fig. 2. The sinusoidal fringe pattern on digital micromirror device (DMD, DLP LightCrafter 4500, Texas Instruments) is de-magnified and projected onto the specimen. Backscattered light from the specimen is directly imaged onto the CCD camera (Point Gray Grasshop3 GS3-U3-51S5C). The illumination uses white light which comprises three monochromatic components of the wavelengths of 623 nm, 540 nm and 460 nm, respectively. One millimeter on the specimen surface corresponds to 60 pixels on the CCD. The full usable image window is 40mmx25mm. The power of the incident beam on the surface of the specimen was measured by a power meter (OPHIR, NOVA II, Israel) to be ~0.01mW/cm^2 in all three channels. Other details of the setup is similar to the one reported [18].

Biomedical Optics EXPRESS

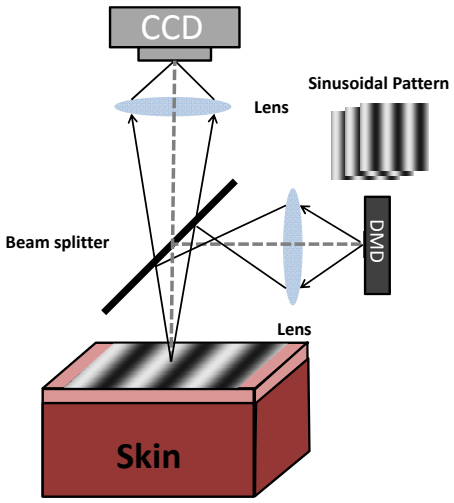

Fig. 2. Schematic diagram of the SSMD-SFDI imaging system.

As the output light intensity from the DMD is not uniform over the whole field of view, calibration was first performed to correct this nonuniformity under planar illumination of a Lambertian reflectance standard. Furthermore, color correction was performed as outlined in Sec 2.3 to remove the cross-contamination between the three (RGB) channels of the digital camera. The accuracy in the recovery of absorption and reduced scattering coefficients was found to be within 1% of the nominal values when imaging a solid tissue phantom (Biomimic, Canada).

The SSMD-SFDI system was used to image the forearms of healthy volunteers (n = 6) under the forearm reactive hyperemia protocol. The spatial modulation frequency of the illumination white light is 0.2 mm^{-1}. The CCD exposure time was fixed at 20000 μs. The SNR for the recorded intensity at one single pixel is approximately 28dB. The measurement for each subject is conducted for 2 minutes before occlusion, 4 minutes during occlusion (cuff pressure: 200 mmHg), and 3 minutes after cuff release at the rate of 3 images per second.

A region of interest (ROI) of size 5mmx5mm within the image window was selected for data analysis. At each temporal point, Single Snapshot Multiple Frequency Demodulation (SSMD) was used to compute the modulation transfer functions, $MTF_{DC} = I_{DC} / I_{DC}^{(0)}$ and $MTF_{AC} = I_{AC} / I_{AC}^{(0)}$, at the spatial frequencies f=0 and 0.2 mm^{-1} for red, green, and blue light from the recorded color image over the ROI. The properties of the two-layer skin including oxy- and deoxyhemoglobin concentrations, the reduced scattering coefficient at 540 nm, the scattering power, the melanin concentration, and the epidermal thickness are then fitted using the function fmincon in Matlab by minimizing the least squared error:

$$error = \sum_{i=1}^{3}\left[\left(MTF_{AC}(\lambda_i) - mtf_{AC}(\lambda_i)\right)^2 + \left(MTF_{DC}(\lambda_i) - mtf_{DC}(\lambda_i)\right)^2\right] \quad (14)$$

where i = 1,2,3 represent the three colors and the theoretical values of the modulation transfer functions MTF_{DC} and MTF_{AC} are computed with the enhanced diffusion model for the effective homogeneous medium [20, 21].

3. Results

Figure 3 shows oxygenated hemoglobin concentration, deoxygenated hemoglobin concentration, total hemoglobin concentration; and blood oxygen saturation for a typical

Biomedical Optics EXPRESS

subject under the forearm reactive hyperemia protocol. As the cuff stopped both venous and arterial blood flow, the total hemoglobin concentration (HbO_2 + Hb, (Fig. 3(c)) remained mostly constant. The expected gradual depletion of oxygen from blood during occlusion resulted in decreasing tissue oxygenated hemoglobin concentration (HbO_2, Fig. 3(a)) and increasing tissue deoxygenated hemoglobin concentration (Hb, Fig. 3(b)). Arterial occlusions are typically characterized by a hyperemic response that a large bolus of oxyhemoglobin inflows upon cuff release to accommodate the high demand for oxygen in tissue which has been depleted during the occlusion period. Such hyperemic response was evident (Fig. 3(a)). The tissue oxygen saturation (StO_2) is 0.82 initially, drops to 0.56 during occlusion, and finally rises to 0.85 rapidly upon cuff release. It is worth noting that the maximum oxygen saturation after cuff release is higher than the initial saturation for all 6 subjects in this study.

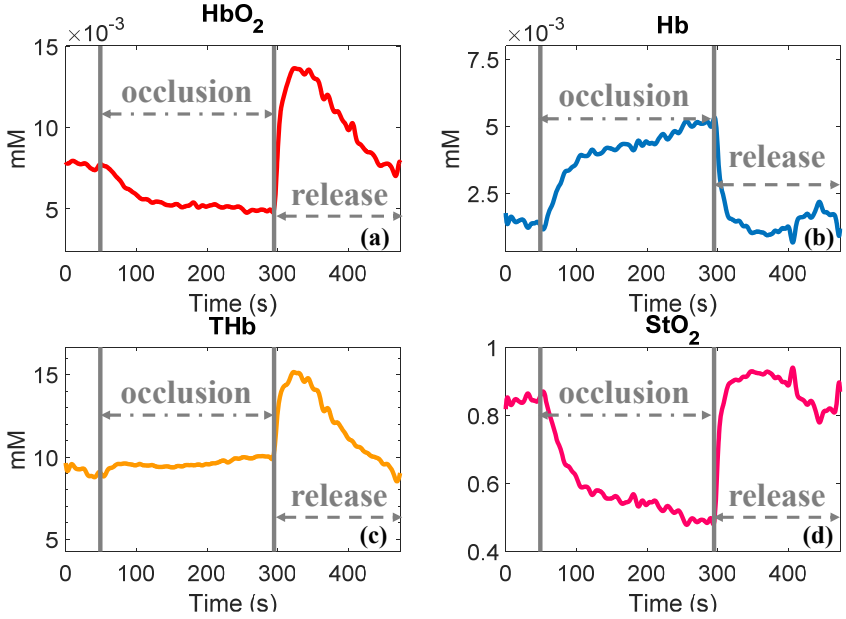

Fig. 3. (a) Oxygenated hemoglobin concentration, (b) deoxygenated hemoglobin concentration, (c) total hemoglobin concentration, and (d) blood oxygen saturation for a typical subject under the forearm reactive hyperemia protocol.

Melanin content and epidermal thickness were basically stable at 3.47 mM and 121 μm (Fig. 4) during the whole experimental period under the forearm reactive hyperemia protocol. The absorption coefficient of epidermis and dermis, the scattering coefficient at 540nm, and the scattering power for the same subject are shown in Fig. 5. We would like to note that the concentration of melanin corresponds to ~1 g/L (molar mass: 318 g/mol for melanin) and an absorption coefficient of 0.4-1.1 mm^{-1} for red, green and blue light. This agrees with the range of melanin absorption reported by Yudovsky et al [27] for lightly pigmented skin (the melanin absorption is 0.27 mm^{-1} at 694 nm for the concentration 3.47 mM).

Biomedical Optics EXPRESS

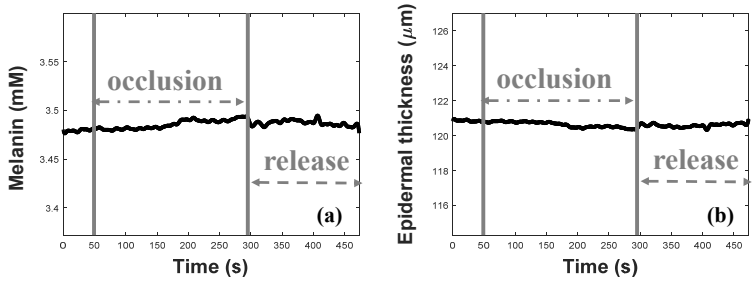

Fig. 4. The recovered melanin concentration and the epidermal thickness under the forearm reactive hyperemia protocol.

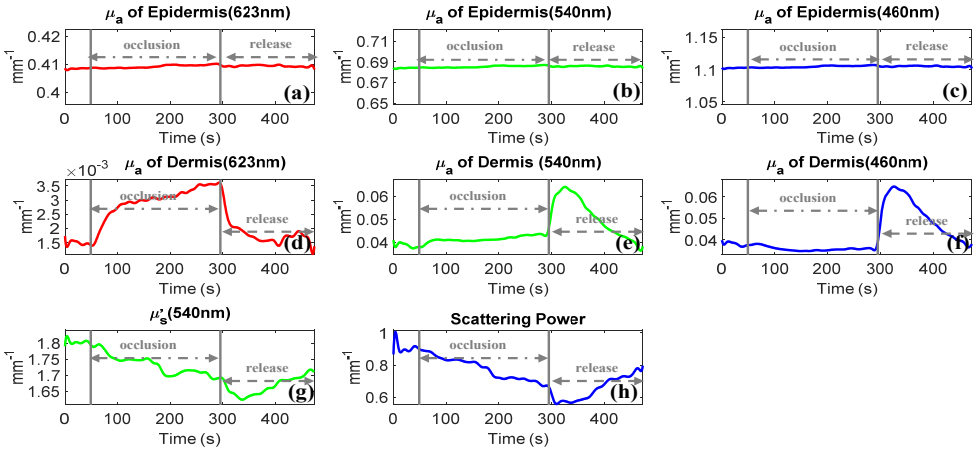

Fig. 5. The absorption coefficient of epidermis (a-c) and dermis (d-f), the scattering coefficient at 540 nm (g), and the scattering power (h) for the same subject under the forearm reactive hyperemia protocol.

The average oxy- and deoxy-hemoglobin concentration, melanin content, epidermal thickness, the scattering coefficient (540 nm) and the scattering power for six volunteers (2 males and 4 females) during baseline, occlusion, and release states are summarized in Fig. 6. The values for each individuals are computed by averaging over one minute immediately before cuff for the baseline, the last minute during cuff for the occlusion state, and the first minute immediately after cuff release for the release state. The standard deviations computed among the 6 subjects are also shown. The *p*-values from *t*-tests on these parameters during baseline, occlusion, and release states are listed in Table 3. It confirmed the same trend observed in Figs. (3-5) that on average tissue oxyhemoglobin concentration decreased while tissue hypoxia hemoglobin concentration and oxygen saturation increased due to cuff (from the baseline to the occlusion state). Upon cuff release, tissue oxygenated hemoglobin concentration and oxygen saturation rose rapidly whereas tissue hypoxia hemoglobin concentration decreased. Melanin and epidermal thickness remained unchanged during the experiment as expected while scattering parameter and scattering power declined steadily.

Biomedical Optics EXPRESS

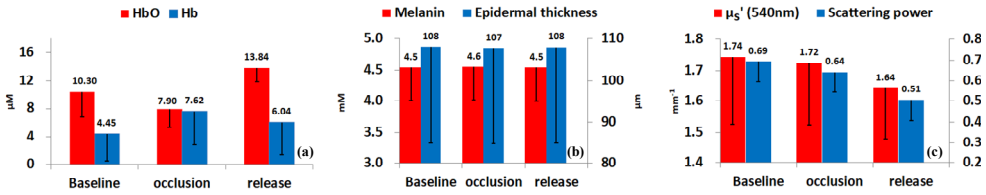

Fig. 6. The average oxy- and deoxy-hemoglobin concentration, melanin content, epidermal thickness, the scattering coefficient (540 nm) and the scattering power for six volunteers (2 males and 4 females) during baseline, occlusion, and release states. The values for each individual are computed by averaging over one minute immediately before cuff for the baseline, the last minute during cuff for the occlusion state, and the first minute immediately after cuff release for the release state.

Table 3. The *p*-values from *t*-tests on the average oxy-, deoxy-, and total hemoglobin concentrations, melanin content, epidermal thickness, the scattering coefficient (540 nm) and the scattering power during baseline, occlusion, and release states.

	HbO2	Hb	THb	Melanin	$\mu_s'(540\,\mathrm{nm})$	Scattering power	Epidermal thickness
Baseline vs Occlusion	0.0253	0.0347	0.5027	0.2242	0.3917	0.2819	0.1116
Occlusion vs Release	0.0004	0.3278	0.0180	0.6835	0.0303	0.0085	0.6020
Baseline vs Release	0.0240	0.1911	0.0010	0.8991	0.0699	0.0200	0.8534

To validate the two-layer model used in the above analysis, we have performed Monte Carlo simulations [36] to compare light reflectance from the two-layer structure and the mapped homogeneous medium. The two-layer structure consists of a top layer of thickness 0.1mm with melanin concentration of 3.485 mM and a bottom semi-infinite layer containing 0.0077mM HbO_2 and 0.0027mM Hb. The reduced scattering coefficient was assumed to be 1.70mm^{-1} at 540nm, the scattering power 0.76, the refractive index 1.40, and the anisotropy factor 0.7 throughout the two-layer structure [37]. Incident light was normal to the surface and light emerging from the medium within 5 degrees from the normal direction was recorded. Five million photons were launched for one single simulation inside the two-layer structure or the mapped homogeneous medium. Each simulation is repeated five times to compute the standard deviation. Figure 7(a) shows the reflectance simulated with the above two-layer structure and the equivalent homogeneous medium. Good agreement is observed between the two models with a slightly larger error near DC. The average maximum penetration depth of spatially modulated light is shown in Fig. 7(b). Visible light is found to be mostly confined within the epidermis and dermis layer of the skin and is insensitive to the subcutaneous layer below. The application of the visible light in skin imaging is hence advantageous by suppressing the interference from tissues beneath.

Biomedical Optics EXPRESS

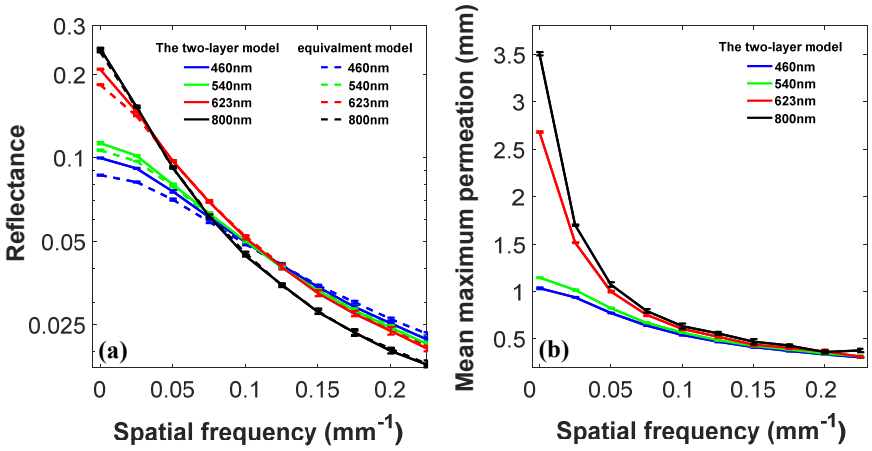

Fig. 7. (a) The reflectance simulated with the two-layer structure and the equivalent homogeneous medium. The error bars show the standard deviation from five repeated simulations. (b) Mean maximum penetration of the spatially modulated light at wavelengths of 460 nm, 540 nm, 623 nm and 800 nm.

4. Discussion

We have presented a noncontact imaging technique SSMD-SFDI, which is capable of mapping optical properties (absorption and scattering coefficients μ_a and μ_s', and scattering power) and physiological parameters including hemoglobin concentration, oxygen saturation, melanin content and epidermal thickness over a large field of view for skin in real time. By applying our single-shot demodulation technique SSMD, the optical properties and physiological parameters are obtained from a single-frame of color image after proper color correction, which overcomes the potential issues of imaging speed and motion artifacts associated with the conventional SFDI using three-phase demodulation.

One key step in our single snapshot imaging of the skin is the introduction of a novel method mapping the two-layer structure to an effective homogeneous medium for SFDI. Although the reduced scattering coefficient of the epidermis is slightly larger than that of the dermis [37], the assumption of an identical scattering property shared throughout the skin is well justified due to the fact that the epidermis is thin (~100 μm) and light is still approximately collimated after passing through the epidermis. The absorption coefficient of the mapped effective homogeneous medium is determined by enforcing an identical amount of absorption for a typical photon migrating in either medium, similar to Saager et al [28]. Comparing with the two-layer model proposed earlier [28], the new approach has some significant advantages that the varying penetration depth of spatially modulated light at different modulation frequencies is taken into account and the imaging can be performed in real time. The usage of visible light also enables higher sensitivities to chromophores of interest. The performance of this two-layer model may be witnessed by the stability of the recovered melanin content and epidermal thickness during the whole reactive hyperemia protocol. This two-layer model can be easily extended to multiple-layer systems and may also be applied beyond the skin in modeling other layered structures such as stratified epithelium and superficial stroma [38].

We note that the accuracy of the proposed two-layer model increases with the spatial modulation frequency and it contains a slightly larger error near DC. The crosstalk between scattering and absorption parameters has also long been an important issue in SFDI. These difficulties are minimized by several steps taken in our system and data analysis. The use of the visible spectrum range in our system gives rise to much stronger spectral variation and absorption strength by chromophores than that within the commonly used NIR range.

Biomedical Optics EXPRESS

Furthermore, the chromophore concentrations are directly recovered via Eq. (14) rather than through a two-step process in which the absorption coefficients were first fitted and then the Beer's law was used to compute the chromophore concentrations afterwards.

The *in vivo* study of reactive hyperemia demonstrates the ability of SSMD-SFDI to measure intrinsic signals which are relevant to dynamic physiology. We observed the entire physiological process during occlusion. Upon cuff oxygenated hemoglobin concentration decreased accompanied by the increasing hypoxia hemoglobin concentration.

To analyze the physiology involved, we estimated the oxygen partial pressure value (PO_2) from oxygen saturation (StO_2) based on the oxygen dissociation curve. PO_2 indicates the blood oxygen concentration that can be used directly by the tissue cells. In the first descending phase of StO_2 (84 (Red dot) to 59 (Green dot) in Fig. 8), StO_2 and PO_2 decreased rapidly, indicating there was a rapid oxygen consumption. The blood oxygen concentration initially was unable to sustain the tissue cells' normal oxygen metabolism. To avoid hypoxia, aerobic cells reduced the level of oxygen metabolism by self-regulation. Part of cell functions changed from aerobic metabolism to anaerobic metabolism. In the second descending phase of StO_2 (59 (Green dot) to 49 (blue dot) in Fig. 8), the level of oxygen metabolism gradually decreased to a stable state and cell activity was essentially static. HbO_2 released oxygen uniformly and PO_2 declined slowly. The tissue cells will eventually reach hypoxia with the increase of the cuff time [39].

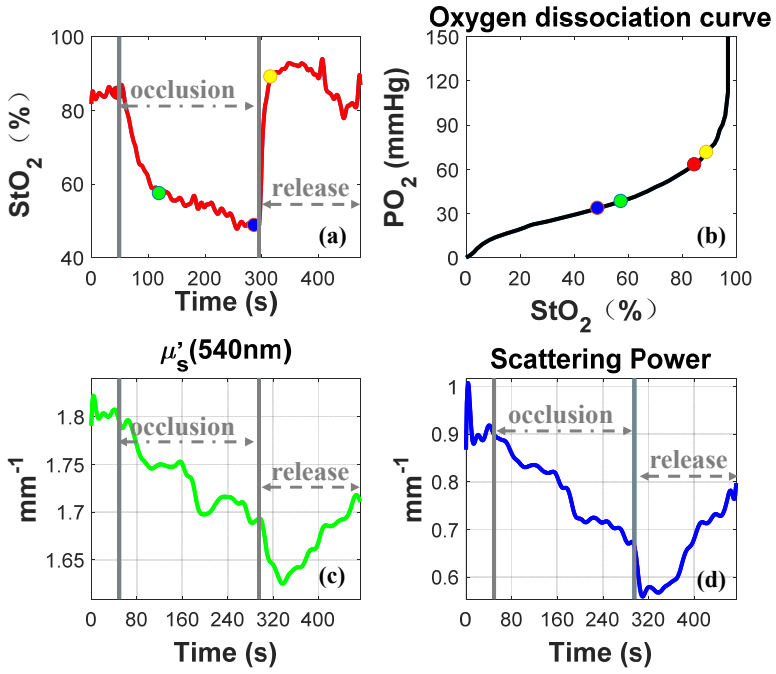

Fig. 8. (a) The hemoglobin concentration, (b) the partial pressure of oxygen, (c) the scattering coefficient at 540 nm, and (d) the scattering power for the same subject under the forearm reactive hyperemia protocol.

During occlusion the reduced scattering coefficient declined with a slightly increasing total tissue hemoglobin concentration, indicating that the blood volume expanded within the probing depth. This may be caused by blood deposition in cutaneous blood vessels due to the venous return being obstructed [40, 41]. We hypothesized that when the cuff blocked the single-arm blood flow, the blood pressure of systemic circulation increased, which further triggered sinusoidal reflex by the baroreceptor and peripheral vasculature dilated reflexively

Biomedical Optics EXPRESS

[42]. Since 200mmHg pressure was enforced by the cuff, no arterial blood flew into the forearm area while the tissue was in acute hypoxia. To meet the needs of distal tissue oxygen consumption, the arterial smooth muscle contracted and relaxed slowly, pumping blood to the aerobic tissue to maintain its basic metabolism [43]. Blood filled into the capillary microcirculation intermittently. Consequently, the reduced scattering coefficient oscillated around the decline trend (Fig. 8(c), 8(d)).

We also note that the scattering properties, unlike hemoglobin concentrations, did not return to the baseline values within the 3 minutes window after cuff release (Figs. 3 and 8). This is not surprising as the former reflects the tissue structural re-organization whereas the latter originates from the fluid (blood).

Since melanin absorbs light strongly, its impact on light migration in skin cannot be ignored. The separation of melanin contribution to light absorption is hence critical to obtain accurate cutaneous hemoglobin concentration and oxygen saturation, important in skin physiology and microcirculation monitoring. The determination of melanin content and the epidermal thickness may be useful in distinguishing melanoma caused by abnormal melanoma cell proliferation [44] from the normal pigmented nevus. In addition, it is beneficial to study the skin pigmentation and metabolic control in patients with type 1 diabetes mellitus, the correlation of microvascular disease, and the detection of vitiligo observed in diabetic patients [45].

In summary, the proposed SSMD-SFDI platform and the two-layer skin mapping method have great potential in monitoring skin structure and cutaneous microcirculation including the blood hemoglobin concentration, oxygen concentration, scattering properties, melanin content and epidermal thickness. In the future work, we expect to increase the sampling rate from 3 fps to 50 fps and provide the two-dimensional images of physiological parameters in real time. The spatial and temporal dynamics of the physiological parameters may gain deeper insight into skin structure and cutaneous microcirculation.

Funding

National Natural Science Foundation of China (81470081); Key Research Program of Zhejiang Natural Science Foundation of China (LZ16H180002); US National Science Foundation (NSF) (1607664); Wenzhou Science and Technology Major Project (ZS2017022) and Zhejiang Xinmiao Talents Program (2016R413076).

Disclosures

We report a patent application related to the technology and analysis methods described in this study. The authors declare that there are no other conflicts of interest related to this article.